NANO · MICRO small
www.small-journal.com

Fabrication of a Robust PEM Water Electrolyzer Based on Non-Noble Metal Cathode Catalyst: $[Mo_3S_{13}]^{2-}$ Clusters Anchored to N-Doped Carbon Nanotubes

Peter K. R. Holzapfel, Melanie Bühler, Daniel Escalera-López, Markus Bierling, Florian D. Speck, Karl J. J. Mayrhofer, Serhiy Cherevko, Chuyen V. Pham, and Simon Thiele**

High investment costs and a dependence on noble metal catalysts currently obstruct the large-scale implementation of proton exchange membrane water electrolyzers (PEMWEs) for converting fluctuating green electricity into chemical energy via water splitting. In this context, this work presents a high-performing and stable non-noble metal catalyst for the hydrogen evolution reaction (HER), consisting of $[Mo_3S_{13}]^{2-}$ clusters supported on nitrogen doped carbon nanotubes (NCNTs). Strikingly, a significant electrochemically induced activation of the Mo_3S_{13}-NCNT catalyst at high current densities is observed in full cell configuration, enabling a remarkable current density of 4 A cm^{-2} at a cell voltage of 2.36 V. To the authors' knowledge, this is the highest reported value to date for a PEMWE full cell using a non-noble metal HER catalyst. Furthermore, only a minor degradation of 83 μV h^{-1} is observed during a stability test of 100 h constant current at 1 A cm^{-2}, with a nearly unchanged polarization behavior after the current hold. Catalyst stability and activity are additionally analyzed via online dissolution measurements. X-ray photoelectron spectroscopy examination of the catalyst before and after electrochemical application reveals a correlation between the electrochemical activation occurring via electrodissolution with changes in the molecular structure of the Mo_3S_{13}-NCNT catalyst.

1. Introduction

Using surplus electricity from fluctuating renewable energy sources to generate hydrogen via water electrolysis combined with hydrogen storage could play a key role in the transition toward a carbon neutral energy system.[1–4] Currently two electrolysis technologies, capable of directly utilizing electricity for water splitting, are available on a large scale commercial level: alkaline water electrolysis and proton exchange membrane water electrolysis (PEMWE).[5] PEMWE has a higher tolerance to differential pressures and current fluctuations as well as system shutdowns and cold-starts.[6–9] Consequently, PEMWE can be better coupled with fluctuating energy sources and electrochemical hydrogen compression.[5,10,11] Main drawbacks of proton exchange membrane (PEM) electrolyzers are the comparably high investment costs and the need for platinum group metals (PGMs) electrocatalysts: namely iridium and platinum.[5,6] Even though the costs for catalyst only account for ≈8% of a PEMWE stack and ≈5% of the overall PEMWE system costs, the limited availability of PGMs could hinder the implementation of PEMWE on a terawatt scale.[5,6] Therefore, the discovery and evaluation of PGM-free catalysts for PEM water electrolysis is a pressing matter for the realization of a hydrogen based energy economy.

For both the oxygen evolution reaction (OER) at the anode and the hydrogen evolution reaction (HER) on the cathode side, numerous reports exist targeting the reduction of PGMs in the catalyst layer.[9,12] The reduction is mainly realized via the use of high surface catalyst supports, such as carbon as platinum support for the cathode side and titanium as iridium support

P. K. R. Holzapfel, Dr. D. Escalera-López, M. Bierling, F. D. Speck, Prof. K. J. J. Mayrhofer, Dr. S. Cherevko, Prof. S. Thiele
Forschungszentrum Jülich GmbH
Helmholtz Institute Erlangen-Nürnberg for Renewable Energy (IEK-11)
Egerlandstr. 3, Erlangen 91058, Germany
E-mail: si.thiele@fz-juelich.de

The ORCID identification number(s) for the author(s) of this article can be found under https://doi.org/10.1002/smll.202003161.

DOI: 10.1002/smll.202003161

P. K. R. Holzapfel
Technische Universität Berlin
Chair of Sustainable Engineering
Str. des 17. Juni 135, Berlin 10623, Germany
Dr. M. Bühler
Hahn-Schickard
Georges-Koehler-Allee 103, Freiburg 79110, Germany
Dr. M. Bühler, Dr. C. V. Pham
Electrochemical Energy Systems
IMTEK - Department of Microsystems Engineering
University of Freiburg
Georges-Koehler-Allee 103, Freiburg 79110, Germany
E-mail: chuyen.pham@imtek.uni-freiburg.de
Prof. K. J. J. Mayrhofer, Prof. S. Thiele
Department of Chemical and Biological Engineering
Friedrich-Alexander-Universität Erlangen-Nürnberg
Egerlandstr. 3, Erlangen 91058, Germany

on the anode side.[9,13,14] Concerning the complete substitution of PGM catalysts in PEMWE, only few examples are available: PGM-free OER catalysts in acidic media such as manganese oxide, crystalline nickel manganese antimonates, and nitrogen-doped tungsten carbide nanoarrays have shown promising performances.[15–18] However, especially for manganese based catalysts, stability seems to be insufficient for practical electrolysis application.[17] Promising PGM-free HER catalysts in acidic conditions are cobalt phosphide (CoP), molybdenum sulfide (MoS_x), molybdenum phosphide (MoP), usually supported onto carbon black, as well as CuMo and NiMo.[19–24] Only few studies report a full cell performance analysis of PEMWE membrane electrode assemblies (MEAs) using PGM-free HER catalysts.[19,25–29] To our knowledge, the highest performances of a PEMWE cell using a non-noble metal HER catalyst was obtained by Jaramilo's group, who tested and compared three MoS/MoP on carbon black (CB) catalysts.[19] Best performance was achieved for MoP|S-CB, which reached current densities of up to ≈1.2 A cm^{-2}. In this research, 3 mg cm^{-2} of MoP|S-CB were used as cathodic catalyst and 2 mg cm^{-2} iridium black were used as anodic catalyst. The catalyst layers were deposited on a Nafion 115 membrane. The same group recently further demonstrated a promising result of CoP as an HER catalyst in a commercial-scale PEM electrolyzer that showed a stable operation at a current density of 1.86 A cm^{-2} for >1700 h.[29] This is an encouraging result, proving the viability of PGM-free HER catalysts in practical applications. Since the applied cell voltage of 2.3 V to reach this current density in that study was still relatively high compared to MEAs using platinum based cathodes, further developments to enhance the electrochemical performance of electrolyzers with PGM-free cathodes are needed.

In this research we present a hybrid of $[Mo_3S_{13}]^{2-}$ nanoclusters supported on nitrogen-doped carbon nanotubes (Mo_3S_{13}-NCNT) as HER catalysts. The formation of the Mo_3S_{13}-NCNT catalyst is assumed to be based on a self-assembly process due to the high chemical affinity of Mo to N-dopants of NCNTs. In our research, we investigate the electrochemical performance toward the HER in a rotating disk electrode (RDE) setup and characterize the catalyst in terms of chemical structure and morphology. To fully assess its practical application and gain insights into the optimal catalyst utilization in a PEMWE cell, we prepared MEAs with four different Mo_3S_{13}-NCNT catalyst loadings (loading based only on $[Mo_3S_{13}]^{2-}$ = 1.6, 3.0, 4.5, 5.8 mg cm^{-2}) and characterized them in a full cell setup. The cell with 3 mg cm^{-2} cathode catalyst loading delivered a stable current density of 1 A cm^{-2} at 1.93 V after a 100 h current hold and reached a current density of 4 A cm^{-2} at 2.36 V. To gain more insights in the activation and stability of the Mo_3S_{13}-NCNT catalyst on both catalyst and full cell level, an in situ dissolution analysis using a scanning flow cell in combination with inductively coupled plasma mass spectrometry (SFC ICP-MS) was performed.

2. Results and Discussions

2.1. Catalyst Characterization

2.1.1. Physical Characterization

$[Mo_3S_{13}]^{2-}$ clusters and Mo_3S_{13}-NCNT hybrid were synthesized as described in the Experimental Section. **Figure 1** shows the morphology of pure NCNTs and Mo_3S_{13}-NCNT hybrids in transmission electron microscope (TEM) images. The $[Mo_3S_{13}]^{2-}$ clusters materials are observably attached to NCNTs, as shown in Figure 1b in comparison with the pure NCNTs presented in Figure 1a. Figure 1c illustrates the chemical structure of the Mo_3S_{13}-NCNT hybrid catalyst. We assume that the forming of Mo_3S_{13}-NCNT hybrids is based on a self-assembly process aided by the chemical affinity of Mo atoms of $[Mo_3S_{13}]^{2-}$ clusters to N atoms of NCNT due to the high electron-negativity of N elements (3.04 by Pauling scale).

The chemical composition of the resulting products was then investigated via X-ray photoelectron spectroscopy (XPS). **Figure 2** presents survey and high-resolution XPS spectra at Mo2p and S2p areas of the pristine $[Mo_3S_{13}]^{2-}$ clusters and Mo_3S_{13}-NCNT. The survey XPS spectra of the two materials are similar showing the presence of the $[Mo_3S_{13}]^{2-}$ clusters in the novel hybrid material. The two spectra contain peaks at 531.0, 413.0, 395.0, 284.0, 229.0, and 163.0 eV, related to the characteristic binding energies of O1s, $Mo3p_{1/2}$, $Mo3p_{3/2}$, the overlapping Mo3d-S2s, and S2p, respectively.[30,31] However, the C1s peak of Mo_3S_{13}-NCNT has a significantly higher relative intensity compared to that of freestanding $[Mo_3S_{13}]^{2-}$ due to the presence of NCNTs in the hybrids. The S/Mo ratios are 4.33 and 3.9 for $[Mo_3S_{13}]^{2-}$ and Mo_3S_{13}-NCNT hybrid, respectively. This is consistent with the S/Mo ratios of chemical formula of $[Mo_3S_{13}]^{2-}$

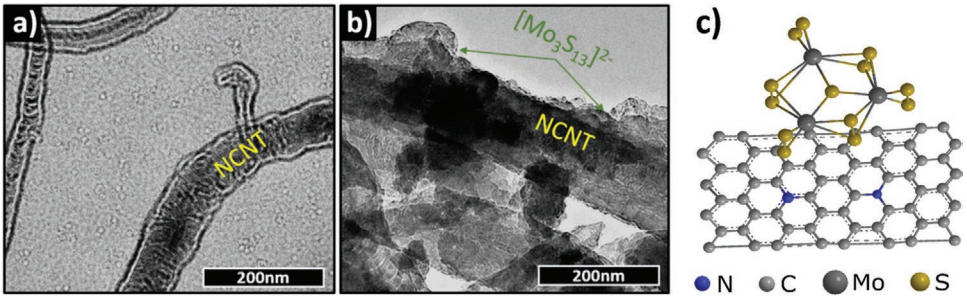

Figure 1. TEM images and chemical structure: a) TEM image of pure NCNT. b) TEM image of Mo_3S_{13}-NCNT hybrid catalyst, showing that there is a modification of the NCNTs in the form of aggregates of the novel material. c) Illustration of the chemical structure of the Mo_3S_{13}-NCNT hybrid catalyst.

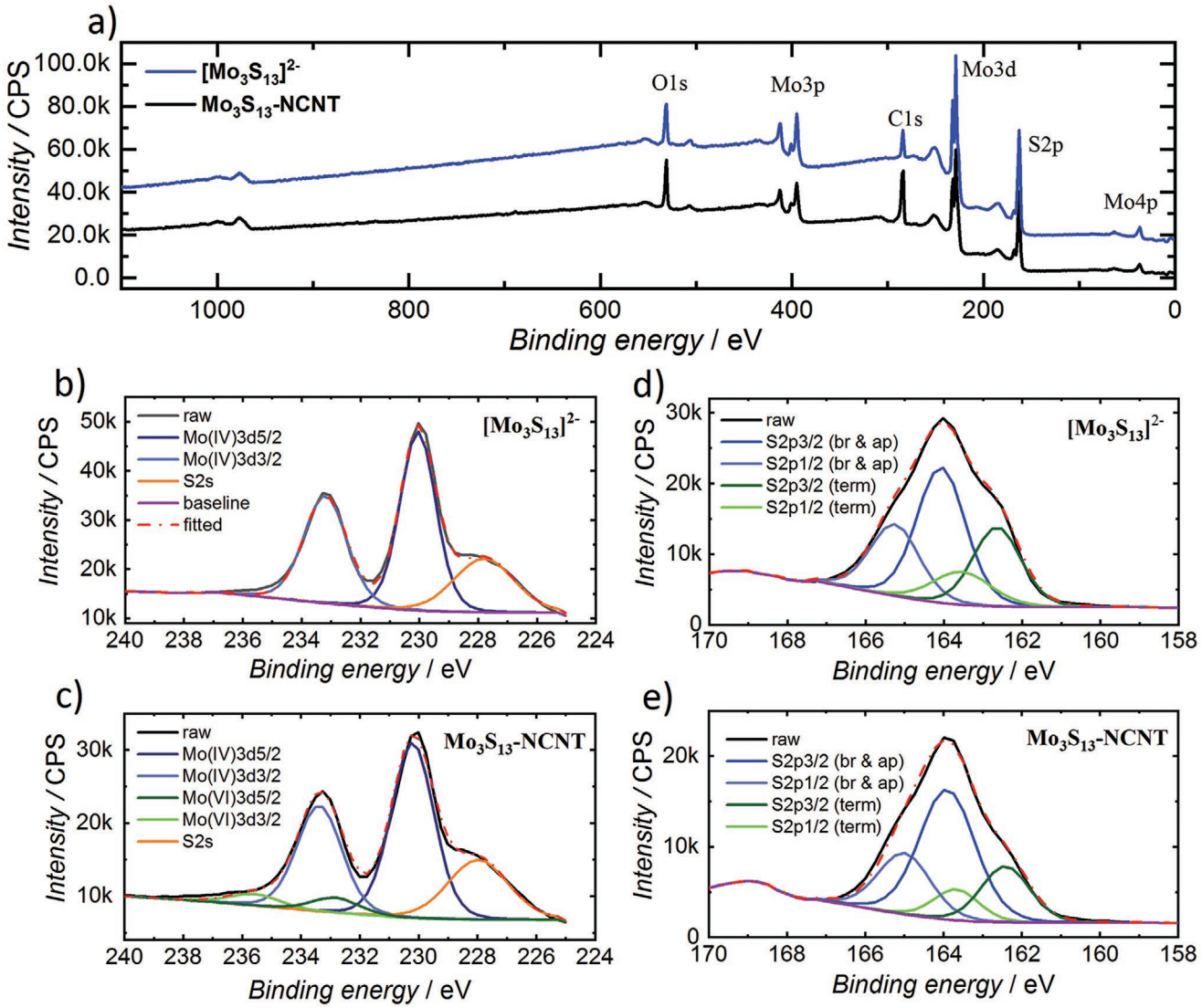

Figure 2. a) XPS survey spectra analysis of freestanding $[Mo_3S_{13}]^{2-}$ clusters and Mo_3S_{13}-NCNT hybrid. b,c) High-resolution deconvoluted XPS spectra of Mo3d and d,e) area of S2p for freestanding $[Mo_3S_{13}]^{2-}$ clusters and Mo_3S_{13}-NCNT hybrid catalyst powders.

clusters. The lower S/Mo ratio of the hybrid can be attributed to the oxidation of some Mo atoms, leading to the removal of some S atoms during the treatment with dimethylformamide (DMF) at 140 °C. The presence of the C-spectra signal in the $[Mo_3S_{13}]^{2-}$ sample is most probably due to the preparation procedure: a carbon-tape was used to glue the sample onto the sample holder. Further information regarding elemental compositions of the two materials are presented in Tables S1 and S2 in the Supporting Information, which are consistent with our previous work.[30]

High-resolution XPS analyses were conducted at Mo3d and S2p areas to elucidate the chemical configurations of Mo and S atoms in both $[Mo_3S_{13}]^{2-}$ and Mo_3S_{13}-NCNT hybrid. Figure 2b,c shows the overlapping peaks of Mo3d and S2s, which were deconvoluted into three peaks, including an S2s component at 228 eV and two doublets of $Mo3d_{3/2}$ (230 eV) and $Mo3d_{5/2}$ (233.5 eV). The doublet peak is attributed to Mo with +4 oxidation state, occurring in $Mo^{IV}(S–S)_3(\mu S)$ structures, where $(S–S)^{2-}$ and μS units are assigned for bridging disulfide and apical sulfide, respectively.[30,32] The additional small doublet peaks at 236 and 233 eV in the Mo3d spectra of Mo_3S_{13}-NCNT hybrid (Figure 2c) can be ascribed to MoO_3 byproducts arising from DMF treatment, absent in the Mo3d region of the pristine $[Mo_3S_{13}]^{2-}$ clusters (Figure 2b). This explains for the lower S/Mo ratio of Mo_3S_{13}-NCNT compared to $[Mo_3S_{13}]^{2-}$ as mentioned above. Likewise, the S2p peaks of both materials are resolved into two doublets ($2p_{3/2}$ and $2p_{1/2}$, $2p_{3/2}$ peak with two times higher intensity than $2p_{1/2}$ peak). One doublet at 162.5 and 163.5 eV associates with $(S–S)^{2-}$ bridging and μS apical, and the other doublet at 164.1 and 165.2 eV attributes to terminal sulfur ligands (Figure 2d,e). The ratio of $(S–S)^{2-}$ bridging and μS apical to terminal sulfur ligands (S-ratio) is 2.5, consistent for both catalysts (Table S3, Supporting Information). As the theoretical S-ratio of a $[Mo_3S_{13}]^{2-}$ cluster equals 6 bridging S plus 1 apical S/6 terminal S = 1.17, we attributed the high S-ratio to the residual polysulfide from the synthesis precursor. Moreover,

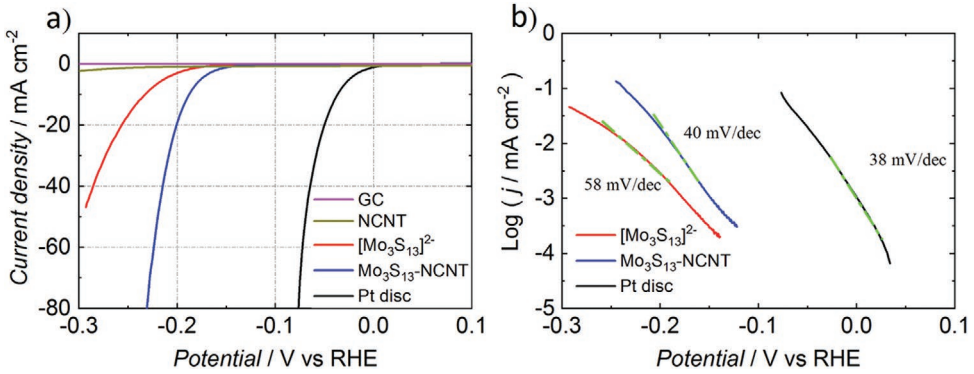

Figure 3. Electrochemical characterization: a) LSV curves of $[Mo_3S_{13}]^{2-}$ clusters, Mo_3S_{13}-NCNT, Pt disk, and glassy carbon disk in N_2-saturated 0.5 M H_2SO_4. b) Tafel plots for the LSVs shown in (a). LSV curves are averaged from positive and negative scanning curves and iR contributions were subtracted. Scan rate: 15 mV s^{-1}.

$[Mo_3S_{13}]^{2-}$ clusters powder exhibited Raman spectrum with a distinct finger-print from 200–600 cm^{-1} (Figure S1, Supporting Information), which was consistent with previous reports.[30,32] Overall, the successful anchoring of $[Mo_3S_{13}]^{2-}$ onto NCNTs as well as the almost unaltered stoichiometry of the nanocluster structure are demonstrated for both freestanding $[Mo_3S_{13}]^{2-}$ clusters and in Mo_3S_{13}-NCNT hybrid in agreement with previous works.[30,32]

2.1.2. Electrochemical Activity

HER activity of freestanding $[Mo_3S_{13}]^{2-}$ clusters and Mo_3S_{13}-NCNT was first studied using a half-cell setup in N_2-saturated 0.5 M H_2SO_4 solution. **Figure 3**a,b presents the linear sweep voltammograms (LSVs) and Tafel plots generated by $[Mo_3S_{13}]^{2-}$ and Mo_3S_{13}-NCNT catalysts in comparison with a Pt disc reference. Mo_3S_{13}-NCNT exhibited an HER activity of 10 mA cm^{-2} at an overpotential of 188 mV versus reversible hydrogen electrode (RHE) and a Tafel slope of ≈40 mV dec^{-1}. These significantly outperform freestanding $[Mo_3S_{13}]^{2-}$ clusters, which showed an overpotential of 233 mV versus RHE at 10 mA cm^{-2} and a Tafel slope of ≈58 mV dec^{-1}. The improved performance of Mo_3S_{13}-NCNT is attributed to the role of the NCNT support in increasing the electrical conductivity and porosity, and therefore the availability of the active sites of the hybrid catalysts, leading to an enhanced catalyst utilization.[33–35] While Mo_3S_{13}-NCNT produced a Tafel slope comparable to that of the Pt disc reference (38 mV dec^{-1}), the studied catalysts display 150 mV more negative onset-potential compared with Pt reference. These results are consistent with the performances of the catalysts in full cell testing, which will be presented in Section 2.2.

2.2. Full Cell Characterization

The performance of the Mo_3S_{13}-NCNT catalyst for the HER in PEMWE was tested in full cell MEA-configurations with first studying the impact of varying loading of the catalyst on the polarization behavior. In this research step the Mo_3S_{13}-NCNT based cathodes were characterized together with a commercial anodic coated N115 membrane. In a successive step the influence of higher current densities on the Mo_3S_{13}-NCNT based cathodes and their long-term stability were investigated. In this research step, the Mo_3S_{13}-NCNT based cathodes were characterized together with an in-house fabricated anodic porous transport electrode (PTE) and a 50 µm thin N212 membrane.

To identify the optimal Mo_3S_{13}-NCNT catalyst loading, cathodes with four different $[Mo_3S_{13}]^{2-}$ loadings (1.5, 3, 4.5, and 5.8 mg cm^{-2}) were fabricated and tested in a full cell setup. The main finding of the loading variation is that the cell performance reaches a plateau at a catalyst loading of 3 mg cm^{-2}. Beyond this threshold, no significant change in polarization behavior was observed. In addition, even the very thick catalyst layer of the 5.8 mg cm^{-2} sample did not lead to significant mass transport issues during electrolysis operation. To compare the performance of the Mo_3S_{13}-NCNT catalyst in this work with a publication by Ng et al.,[19] a catalyst loading of 3.0 mg cm^{-2} $[Mo_3S_{13}]^{2-}$ was chosen for the high performance and stability analysis in the following. A detailed analysis of the loading variation can be found in Figure S2 in the Supporting Information.

The performance under high current densities and the stability during a constant current hold of the Mo_3S_{13}-NCNT-based cathode with a loading of 3 mg cm^{-2} was compared to a commercial Pt/C-reference cathode with a catalyst loading of 0.5 mg cm^{-2}. A full PTE cell configuration with anodic and cathodic PTEs pressed against a free-standing membrane was used (**Figure 4**a). To study the changes in polarization behavior of the pristine MEA versus the MEA after the 100 h stability test, polarization curves were recorded prior to and after the 100 h current hold (Figure 4c). The MEA using the Mo_3S_{13}-NCNT based cathode delivered a current density of 4 A cm^{-2} at a cell voltage of 2.36 V. To our knowledge, this is an unprecedented high current density reported for a PEMWE cell using a noble metal free HER catalyst (Table S4, Supporting Information). Ng et al.[19] showed a maximum current density of about 1.2 A cm^{-2} at 2 V with their catalyst coated membrane (CCM) using 3 mg cm^{-2} MoP|S-CB as cathode catalyst and an N115 membrane. King et al.[29] demonstrated a maximum current density of around 1.8 A cm^{-2} at 2.3 V when using 1 mg cm^{-2} of a cobalt phosphide (CoP) catalyst for the HER in a full PTE-configuration with an N117 membrane. King et al. however reported a remarkable stability of the CoP-based cathode, when applying a constant current of 1.86 A cm^{-2} for more than 1700 h.

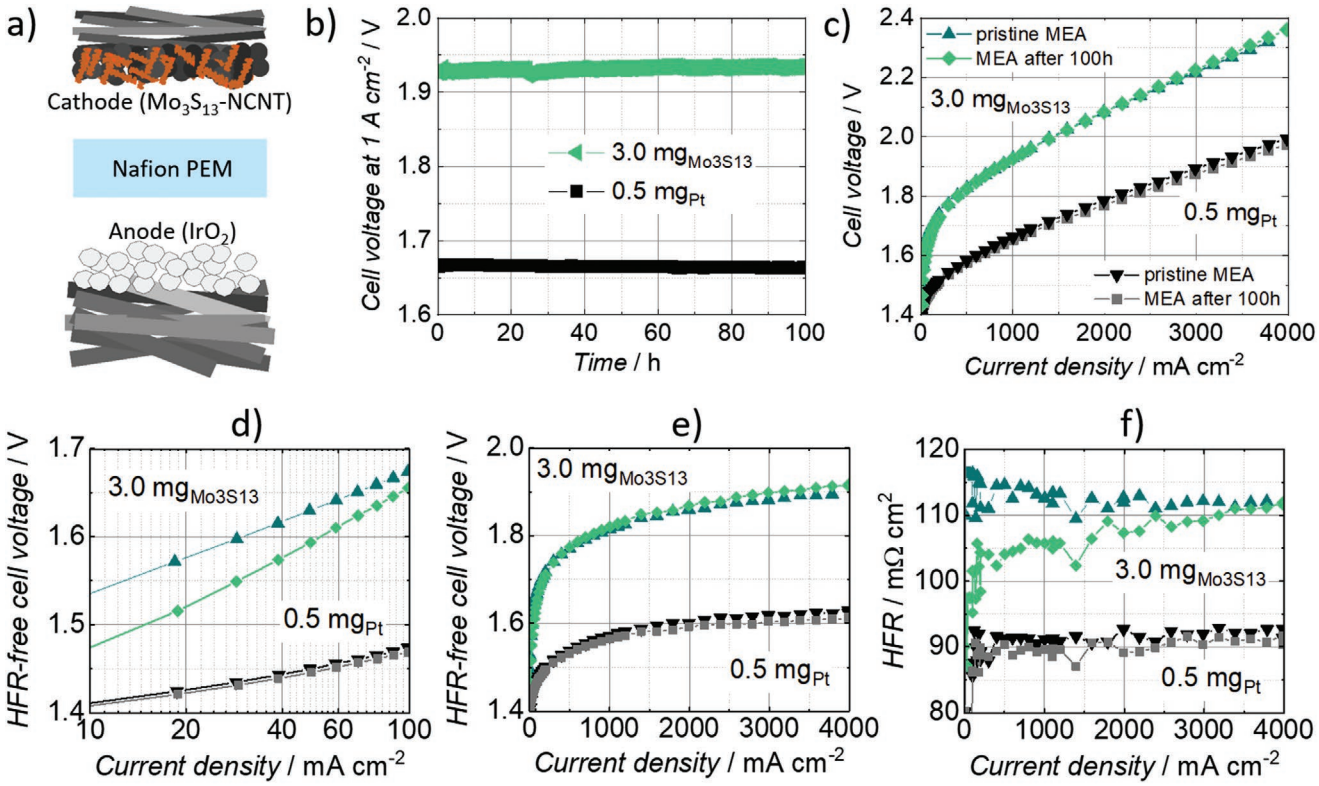

Figure 4. Full cell characterization: a) Schematic illustration of the full cell setup. b) Cell voltage over time during the stability test. c) Polarization data of the pristine MEAs and the same MEAs after the 100 h test. d) HFR-free polarization data at low current densities, plotted on a semi-logarithmic scale. e) HFR-free polarization data and f) HFR over current density.

The cell voltage during the constant current hold (Figure 4b) of the MEA with Mo_3S_{13}-NCNT cathode slightly increased with a rate of 83 µV h^{-1}, which can mainly be attributed to the increase in high frequency resistance (HFR)-free cell voltage (Figure S3a, Supporting Information). The HFR (Figure S3b, Supporting Information) of the Mo_3S_{13}-NCNT cathode stabilized at a value of around 105 mΩ cm^2 after ≈30 h constant current hold. The HFR of the Pt/C-reference was in the range of 88 mΩ cm^2 and showed no significant change during the stability test, which was as well true for the HFR-free cell voltage and thus the overall cell performance. The stability of the Mo_3S_{13}-NCNT cathode presented in this work was superior to the 3 mg cm^{-2} Mo_3S_{13}-CB based cathode in CCM-configuration using an N115 membrane as presented by Ng et al.[19] In their work, Ng et al. held a constant voltage of 1.85 V for 24 h. After the 24 h voltage hold the required cell voltage, to reach 0.5 A cm^{-2}, was increased by 150 mV. The cell voltage at 0.5 A cm^{-2} when using the Mo_3S_{13}-NCNT based cathodes in PTE-configuration in this work was even 2.4 mV lower after the 100 h constant current operation at 1 A cm^{-2}.

Plotting the HFR-free cell voltage on a logarithmic scale in the low current density region (Figure 4d) allows insights to the activation losses of the full cell. The activation losses in the low current density region are reduced after the 100 h current hold for the MEA using the Mo_3S_{13}-NCNT based cathode. This might be due to an additional catalyst activation during the 100 h current hold. However, the HFR-free polarization curve develops with a slightly steeper slope after the current hold, which could be explained by slightly increased mass transport losses. The full HFR-free polarization curve (Figure 4e) reveals slightly higher mass transport losses for the MEA using the Mo_3S_{13}-NCNT based cathode compared to the Pt/C reference which could be the result of the thicker Mo_3S_{13}-NCNT catalyst layer with a six times higher catalyst loading than the Pt/C-reference. The HFR-free cell voltage of the Pt/C-reference slightly improved (decreased) under the 100 h constant current hold, whereas the HFR-free cell voltage of the Mo_3S_{13}-NCNT catalyst based cathode slightly increased. The HFR (Figure 4f) of the Pt/C-reference slightly improved after the 100 h stability test and showed no significant change with increasing current density. The HFR of the Mo_3S_{13}-NCNT based cathode however changed with increasing current density. The pristine MEA showed a reduced HFR with increasing current density, whereas the 100 h operated MEA showed an HFR which was strongly increasing with increasing current density. Both HFRs approached a value of around 112 mΩ cm^2 at the final current density of 4 A cm^{-2} compared with the HFR of the reference MEA of 92 mΩ cm^2. The opposing trend of the pristine versus the MEA after 100 h constant current hold are not yet fully understood and should be investigated in more detail.

2.3. Insight into Electrochemical Activation and Stability

The electrochemical performance of MEAs using the Mo_3S_{13}-NCNT cathode catalyst increased significantly during the cell

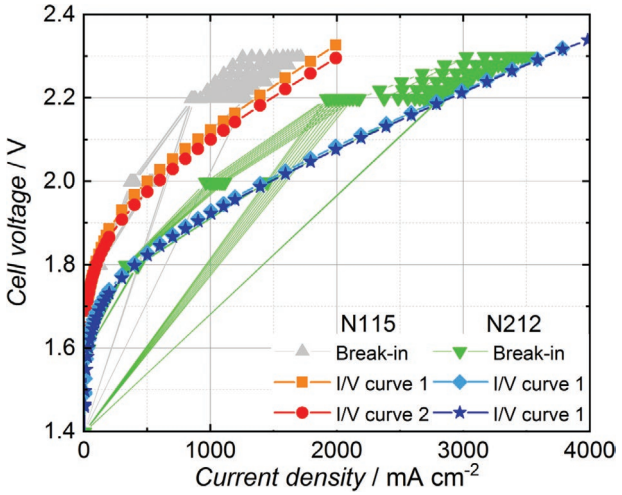

Figure 5. Full cell activation procedure and polarization curves of MEAs using Mo_3S_{13}-NCNT based cathodes (catalyst loading: 3 mg $[Mo_3S_{13}]^{2-}$ cm^{-2}), characterized together with a half-sided anodic coated N115 membrane and in a full PTE setup using an N212 membrane.

activation process (**Figure 5**). Especially when stepping the voltage up from 2.2 to 2.3 V, the corresponding current density increased strongly with each voltage cycle. The performance increase was more significant for the MEA using the thin N212 membrane than for the MEA using a thicker N115 membrane. This is most likely because higher current densities could be reached due to the lower ohmic resistance of the thinner membrane. As can be observed from Figure 5, the current density at 2.2 V increased by 430 mA cm^{-2} during the activation procedure for the MEA using the N115 membrane. For the MEA using the 50 µm thin N212 membrane, the current density increases by 908 mA cm^{-2} at 2.2 V during the activation procedure. We assume that the higher currents, enabled by the lower ohmic resistance of the thinner N212 membrane, led to an enhanced electrochemically induced cluster structure transformation in the Mo_3S_{13}-NCNT cathodes, which resulted in higher electrochemical activity. Hence, the use of the 50 µm thin N212 membrane was crucial to achieving the high cell performance of 4 A cm^{-2} at a cell voltage of 2.36 V. For more detailed information activation process and a performance comparison between MEAs using N115 and N212 membrane respectivly it is referred to Figure S4 in the Supporting Information.

We further evaluated the electrocatalytic stability and activity of both $[Mo_3S_{13}]^{2-}$ and Mo_3S_{13}-NCNT by means of coupling a proprietary three-electrode SFC electrochemical setup downstream to ICP-MS. **Figure 6** shows the electrochemical protocol employed, and the corresponding potential-dependent, as well as real-time Mo dissolution profile detected by ICP-MS. Upon contacting the catalyst spots with the electrolyte at 0 V versus RHE, significant Mo dissolution was detected, higher than that observed under hydrogen evolving conditions or under subsequent holds at 0 V versus RHE (see Figure 6a for total dissolution comparison between 0 V vs RHE holding steps). An analogous behavior was previously reported for crystalline

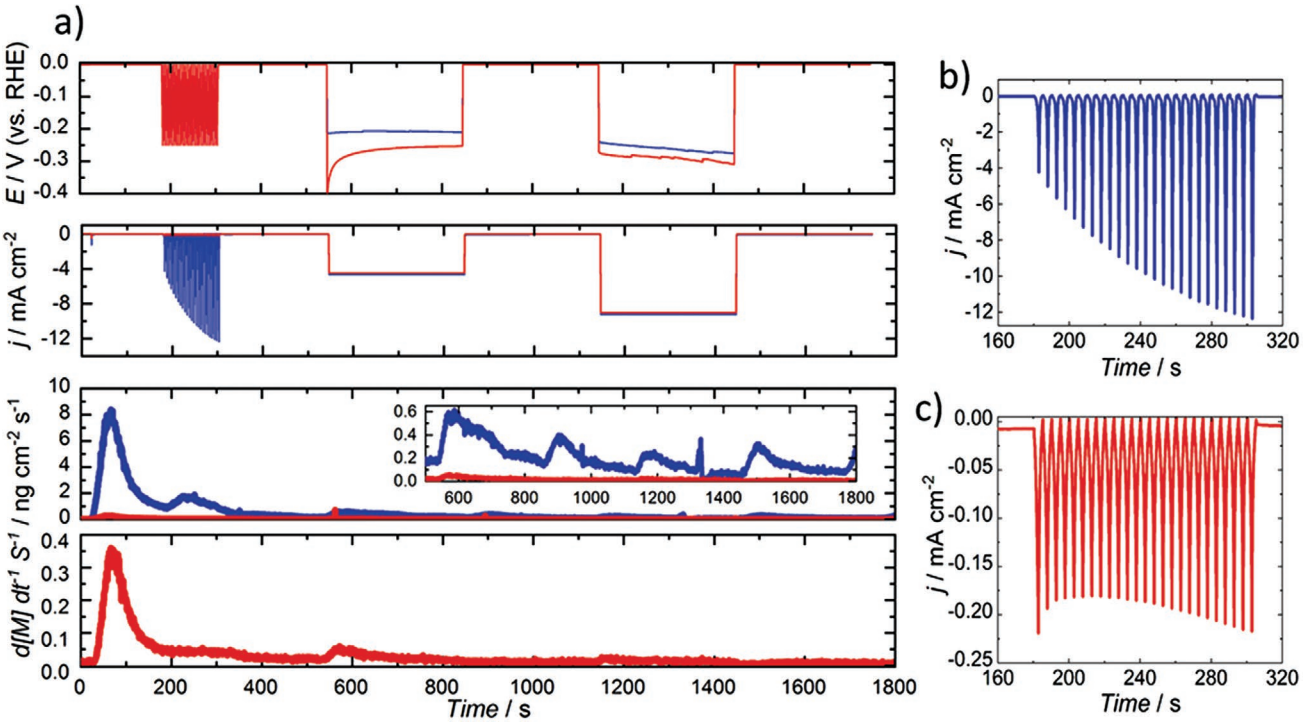

Figure 6. a) Mo online ICP-MS dissolution data recorded for Mo_3S_{13}-NCNT (blue) and freestanding $[Mo_3S_{13}]^{2-}$ (red) during the accelerated potentiodynamic activation cycling (scan rate: 100 mV s^{-1}) and the galvanostatic mass-normalized current holds (potential program vs time shown in top pane and geometric current density vs time shown in second from top pane). For ease of interpretation, Mo ICP-MS dissolution data for $[Mo_3S_{13}]^{2-}$ is individually plotted in the bottom pane. Close-up view of the *j–t* plot obtained during accelerated potentiodynamic activation cycling for b) Mo_3S_{13}-NCNT and c) freestanding $[Mo_3S_{13}]^{2-}$.

MoS_2 upon contacting at open-circuit potential,[36] where Mo dissolution greatly subsided after the first contact with the electrolyte. This can be explained by the presence of undercoordinated Mo moieties, namely S-defects within the Mo_3S_{13} cluster structure, prone to dissolution.[37] Indeed, the higher Mo dissolution found for Mo_3S_{13}-NCNT versus the pristine $[Mo_3S_{13}]^{2-}$ nanoclusters is in good agreement with the lower S/Mo ratio found in the hybrid material (section 2.1): S removal during DMF heating treatment favors the presence of dissolution-prone undercoordinated Mo sites.

An accelerated activation step, consisting of 25 cyclic voltammograms (CVs) from 0 to −0.25 V versus RHE at 100 mV s^{-1} scan rate, yielded an almost threefold increase in HER geometric current densities for Mo_3S_{13}-NCNT (−12.3 vs −4.2 mA cm^{-2}) whereas the pristine $[Mo_3S_{13}]^{2-}$ counterpart showed no improvement (−0.219 vs −0.217 mA cm^{-2}). Mo dissolution signal was, interestingly, higher for Mo_3S_{13}-NCNT (155 ± 29 vs 5 ± 1 ng cm^{-2}) despite the lower $[Mo_3S_{13}]^{2-}$ content in the catalyst (≈66 wt%). We attribute this to the more efficient electron conductive pathway provided by the interconnected NCNTs network, alongside the better $[Mo_3S_{13}]^{2-}$ catalyst dispersion across the working electrode (WE) surface, which yields higher HER currents but also seems to promote the concomitant electrocatalyst dissolution.

Next, two 5 min/5 min start/stop current holds were applied, shifting from mass normalized HER currents of −55.55 mA mg_{cat}^{-1} (−4.7 mA cm^{-2}) and −111.11 mA mg_{cat}^{-1} (−9.2 mA cm^{-2}) and 0 V versus RHE voltage holds, respectively. Higher mass-normalized HER currents were not evaluated given the limitation imposed by the microcapillary SFC regarding surface blockage under copious hydrogen bubble formation mentioned in ref. [38]. The HER overpotentials observed for Mo_3S_{13}-NCNT were consistently lower than those found for the freestanding $[Mo_3S_{13}]^{2-}$ catalyst regardless of the current density observed. The findings are hence in good agreement with the values previously found for RDE experiments: 40 mV at −55.55 mA mg_{cat}^{-1} (−214 ± 8 vs −254 ± 2 mV) and 51 mV at −111.11 mA mg_{cat}^{-1} (−279 ± 22 vs −330 ± 18 mV). Total Mo dissolution is, however, one order of magnitude higher for Mo_3S_{13}-NCNT (60 ± 12 ng cm^{-2} at −55.55 mA mg_{cat}^{-1} hold; 20 ± 8 ng cm^{-2} at −111.11 mA mg_{cat}^{-1} hold) than that observed for freestanding $[Mo_3S_{13}]^{2-}$ (4.2 ± 0.5 ng cm^{-2} at −55.55 A mg_{cat}^{-1} hold; 2.2 ± 0.7 ng cm^{-2} at −111.11 mA mg_{cat}^{-1} hold). We tentatively attribute this to the higher $[Mo_3S_{13}]^{2-}$ dispersion across the NCNTs which also contributes to its improved HER activity and higher dissolution rate as a result.

We now try to shed light on the phenomena behind the electrochemical activation of Mo_3S_{13}-NCNT during full cell and SFC characterization. It is noteworthy that the Mo dissolution profile observed in SFC ICP-MS measurements under fast cycling does not present a steady-state response (Figure 6a). Mo dissolution decay during continuous cycling, despite the clear progression of the electrochemically driven Mo_3S_{13}-NCNT activation, seems to indicate that the activation is not fully ascribable to Mo loss but to another parallel phenomenon. **Figure 7** and Figure S5 in the Supporting Information present the ex situ XPS analysis results of the catalyst spots of Mo_3S_{13}-NCNT and $[Mo_3S_{13}]^{2-}$ respectively, before and after electrochemical testing. It shows that in the high-resolution Mo3d region, an increase in the Mo^{6+} $3d_{5/2:3/2}$ doublet (relative atomic photoemission: 20.8% vs 17.8% and 35.2% vs 25.9% for $[Mo_3S_{13}]^{2-}$ and Mo_3S_{13}-NCNT, respectively). The presence of a Mo^{6+} component on the untested, pristine catalyst (Figure 6a), initially absent in the freshly synthesized catalyst (Figure 2), can be understood given the gradual conversion of Mo^{4+} to Mo^{6+} in $[Mo_3S_{13}]^{2-}$ based catalysts under air-exposure during the storage.[39] This Mo^{6+} component would dissolve quickly as observed when contacting the SFC with the catalyst spots. Therefore, the oxidation of this catalyst, when cathode potential reaches undesired potentials due to, e.g., air-bleed, operation shutdown, could lead to severe degradation.[35] A constant operation is thus recommended.

A relative decrease in the $S2p_{3/2:1/2}$ doublet components is ascribed to $(S–S)^{2-}$ and μS (61.2% vs. 71.4% and 62.4% vs 71.6% for $[Mo_3S_{13}]^{2-}$ and Mo_3S_{13}-NCNT, respectively), suggesting that the cleavage of the bridging S_2^{2-} ligands might be responsible for the HER activation process. This is in line with previous findings concerning this class of catalyst in half cell characterizations.[40–42] However, further investigation on the *postmortem* catalysts collected after full cell tests is needed to fully elucidate the activation process.

3. Conclusion

In this work, we presented Mo_3S_{13}-NCNT as a hybrid catalyst for the HER in PEMWE. The catalyst exhibited an intrinsic activity of 10 mA cm^{-2} at an overpotential of 188 mV and a Tafel slope of ≈40 mV dec^{-1} in RDE half-cell experiments. In full cell measurements, a current density of 4 A cm^{-2} at a cell voltage of 2.36 V was achieved. This current density is, to the best of our knowledge, the highest reported to date when using a non-noble metal based HER catalyst in a full cell PEMWE. Furthermore, the PEMWE cell showed only a minor degradation of 83 μV h^{-1} during a 100 h current hold at 1 A cm^{-2} and an almost unchanged polarization behavior after the current hold. Both full cell and SFC ICP-MS measurements show significant performance improvements with high current densities, which are assumed to originate from an electrochemically induced cluster structure transformation of the Mo_3S_{13}-NCNT catalyst. The use of thinner membranes and an improved protonic interface between catalyst layer and membrane could further promote this effect. Direct membrane deposition, with the possibility to fabricate thin membranes directly on the catalyst layers, is therefore considered as promising design for MEAs using $[Mo_3S_{13}]^{2-}$ based cathodes.[43,44] Further investigations to understand the effect of an electrochemically induced cluster structure transformation on the activity of $[Mo_3S_{13}]^{2-}$ based catalysts are suggested, in order to fully utilize the potential of this catalyst group.

4. Experimental Section

Catalyst Synthesis and Analysis: First, $[Mo_3S_{13}]^{2-}$ clusters were synthesized according to the previous report.[30] For the synthesis of Mo_3S_{13}-NCNT hybrid, 1 g $[Mo_3S_{13}]^{2-}$ clusters and 500 mg nitrogen doped carbon nanotubes (>98%, 5 wt% N, advanced chemicals supplier Materials LLC, USA) were then dispersed in 50 mL DMF

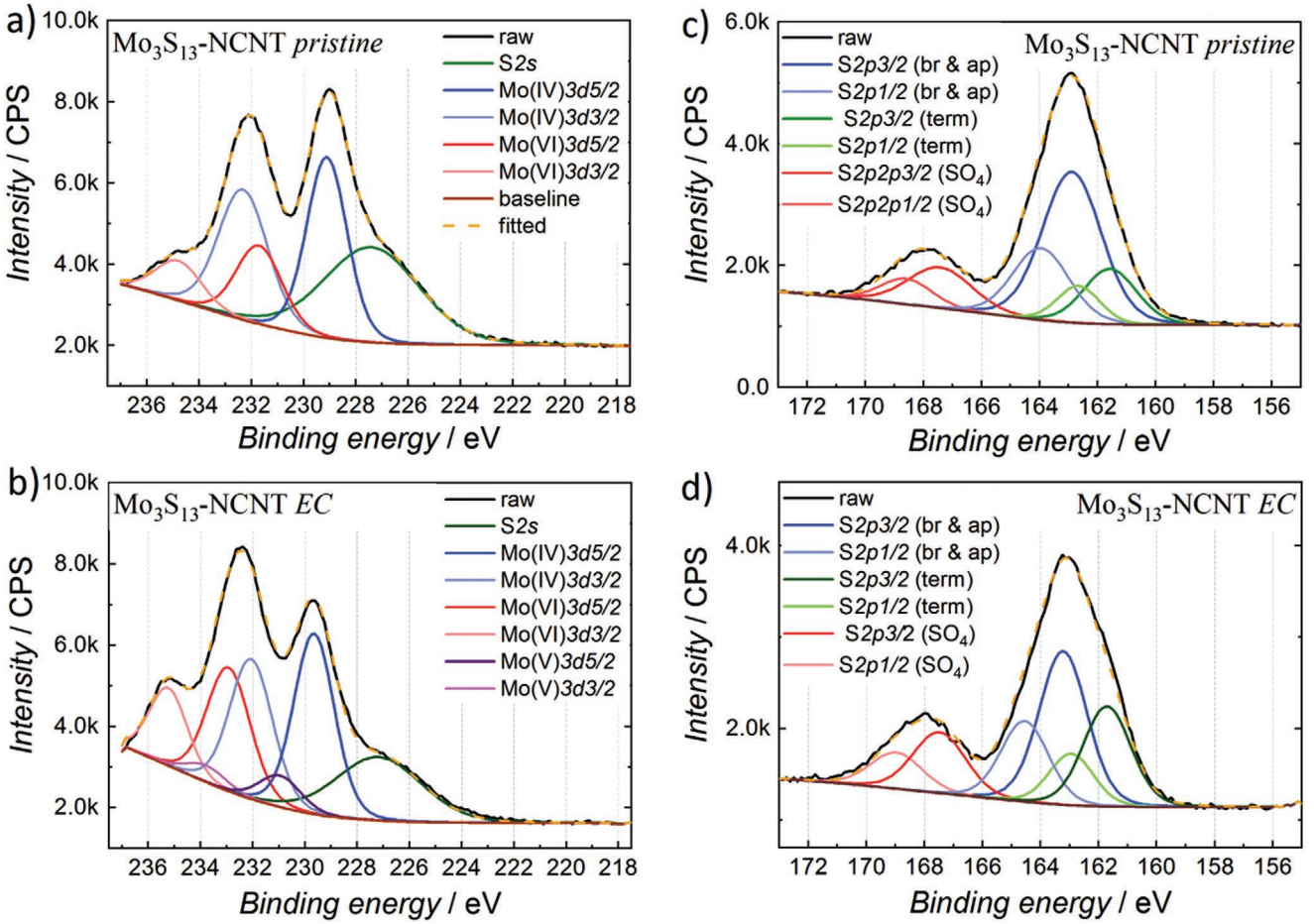

Figure 7. High-resolution deconvoluted XPS spectra of a,b) Mo3d and c,d) S2p for the Mo_3S_{13}-NCNT hybrid catalyst powder a,c) before and b,d) after SFC ICP-MS electrochemical testing.

by ultrasonication for 10 min to obtain a homogeneous dispersion. The dispersion was afterward heat-treated at 140 °C for 24 h under continuous stirring on a magnetic hotplate. Subsequently, DMF solvent was evaporated to dryness using a distillation system under vacuum at 90 °C. Finally, ≈1.5 g of the dried Mo_3S_{13}-NCNT hybrid powder was received and was ground to fine powder using an agate mortar-pestle. Physical and electrochemical characterization was performed on the supported Mo_3S_{13}-NCNT hybrid catalyst and compared to the unsupported $[Mo_3S_{13}]^{2-}$ clusters.

Physical Characterization: For TEM characterization first the catalyst powders were dispersed in isopropanol as solvent. Then TEM samples were prepared by dip-coating TEM grids with the catalyst dispersion, followed by solvent evaporation. The TEM imaging was acquired using a Talos 120C (120 kV, Thermo Scientific). XPS spectra were recorded using a Quantera II. The XPS spectra were analyzed using a CasaXPS software. Quantification analyses were performed with Tougaard background subtraction type and full width at half maximum of each deconvoluted peak being constrained to approximately the same value for the same elements.

Electrochemical Characterization: For RDE measurements, the catalyst inks were prepared by dispersing 10 mg of Mo_3S_{13}-NCNT catalyst and unsupported $[Mo_3S_{13}]^{2-}$ powder for comparison in 1 mL DMF and added 20 µL of Nafion D520 solution (5 wt%, Ion Power) with the help of ultrasonication for 10 min. The testing electrodes were prepared by dropcasting the required amounts of inks onto freshly polished glassy carbon (GC) discs. The GC discs had a diameter of 3 mm and were mounted on an RDE tip (EDI101). The exposed electrode area was 0.07 cm^2. Finally, the catalyst films coated GC were dried in ambient air at 50 °C for about 1 h. The LSV measurements were performed in N_2-saturated 0.5 M H_2SO_4 solutions, which were formed by purging the solutions for 30 min before each measurement. The electrochemical experiments were conducted at room temperature using a three electrode setup: 1) the working electrode, 2) saturated calomel reference electrode, and 3) a GC rod counter electrode. An ECi-200 potentiostat (Nordic electrochemistry) was used to control the electrode potential. A current positive feedback scheme was applied to reach an effective solution resistance of about 1 Ω. The data were recorded and analyzed using EC4TMVIEW software. The speed of the rotating disk electrode (EDI101, Radiometer) was controlled at 1000 rpm to remove H_2 bubbles from the catalyst surface. All potentials reported in this study are referred to the RHE after accounting for the Nernstian shift correction. Measurement data were corrected for contributions of ohmic resistances (iR-corrected).

Full Cell Characterization—Membrane Electrode Assembly: For full cell characterization regarding the variation of the catalyst loading, Mo_3S_{13}-NCNT based catalyst was spray coated onto commercial carbon cloth porous transport layers (PTLs) with microporous layer (GDL-CT, FuelCellsEtc). Spraying the catalyst on a PTL to form a PTE was chosen rather than spraying the catalyst on a membrane, in order to facilitate a homogeneous deposition of relatively thick catalyst layers and to prevent wrinkling of the membrane. To keep the anode side constant for the loading variation, custom-made anodic catalyst coated membranes (anodic CCMs) purchased from FuelCellsEtc, contacted via Ti-fiber sintered PTLs (1 mm thick, 57% porosity, 20 µm fiber diameter, Bekaert) completed the

MEA. The anodic CCMs consisted of a Nafion 115 membrane coated with 1.5 mgIr cm^{-2} of an IrO_2 catalyst for the OER. The applicability of Mo_3S_{13}-NCNT as HER cathode catalyst for high current density applications was characterized in a full PTE-setup. For this, a thinner 50 µm thick Nafion 212 membrane was sandwiched between a cathodic and anodic PTE. The anodic PTEs were the Ti-PTLs directly coated with 1.4 mgIr cm^{-2} of IrO_2 as reported in the previous work.[45] A commercial platinum-based cathodic PTE with a catalyst loading of 0.5 mgPt cm^{-2} (SL-GDE, Pt/C–60 wt% Pt, FuelCellsEtc) served as reference electrode.

To deposit the catalyst layer, a spray coater (Sono-Tek, model Exacta Coat) with an ultrasonic nozzle type AccuMist (48 kHz) was used. The catalyst ink for spray coating the Mo_3S_{13}-NCNT based cathodes consisted of 2 wt% solids and 98 wt% solvents (75 wt% 2-Propanol and 25 wt% de-ionized (DI) water). The solids consisted of 70 wt% Mo_3S_{13}-NCNT, 10 wt% carbon black (Vulcan XC-72R, FuelCellsEtc), and 20 wt% Nafion solids (Nafion D520, FuelCellStore). The catalyst and carbon black was weighed in a glass bottle using a high precision scale. Subsequently DI-water, 2-propanol, and Nafion were added. The glass bottle was slightly agitated after adding each liquid ink component. The catalyst ink was sonicated for 30 min (Hielscher, model UIS250L, 0.55 W, 90% amplitude) while continuously stirring. To ensure a stable temperature, the catalyst ink was placed in an ice bath during the sonication process. The ink was then stirred for 48 h. The sonication procedure was repeated right before spray coating. For spray coating the following parameters were used: path speed of 170 mm sec^{-1}, shaping air of 0.6 kPa, hot plate temperature of 110 °C, 5 W ultrasonic , and flow rate of 0.45 mL min^{-1}. The spray pattern was meander-shaped with a serpentine layer pitch of 1.5 mm and a path offset of 0.75 mm for each second spray path. The nozzle height was set to 37 mm. To monitor the catalyst loading during spray coating, a 1 cm^2 rectangular metal piece was spray coated as well and weighed on a microscale (Sartorius, model ME 36S). Anodic PTEs were fabricated by using the same spray coater and parameters as reported in the previous work.[45]

Electrochemical Performance Analysis: The MEAs were characterized in an in-house designed test cell setup. Two aluminum plates tightened with eight screws (8.5 Nm) held the inner cell parts. The inner cell parts consisted of the MEA clamped between two titanium plates with milled flow fields (5 cm^2 parallel channel structure). Two copper plates were pressed between the Al and Ti plates to establish the electric connection with the potentiostat (Scribner, model 857). The copper plates were electrically insulated from the aluminum. To ensure a stable temperature, a temperature sensor was inserted in the titanium plates and heating elements were inserted into the aluminum plates. The 5 cm^2 PTLs and PTEs were centered in the test cell using PTFE frames. The thickness of the frames set the compression of the porous substrates. For the anode side a 1 mm thick PTFE frame was used and for the cathode side a 150 µm thick PTFE sheet to set the compression of the carbon cloth material to about 60%. Anode and cathode were supplied separately with preheated DI-water via a peristaltic pump (Ismatec, model IP 65) at a flow rate of 40 mL min^{-1}.

Once a stable temperature of 80 °C was observed, the conditioning procedure was initiated. For this, a constant current was held for 5 min at 0.5 A cm^{-2} followed by a voltage scan from 1.4 to 2.2 V in 200 mV steps (30 s per step). Afterward a constant current was applied for 5 min at 0.5 A cm^{-2} followed by a high voltage scan from 2.2 to 2.3 V in 20 mV steps (30 s per step). The third step was a constant current hold for 5 min at 0.5 A cm^{-2} followed by a voltage scan from 1.4 to 2.2 V in 200 mV steps (30 s per step). After a final constant current hold for 5 min at 0.5 A cm^{-2}, each voltage scanning was repeated ten times. Since the current limit of the potentiostat is 20 A, the high voltage scan could not be performed for the MEAs using the highly active Pt/C as cathode catalyst. Following the conditioning procedure, a polarization curve was recorded, using the following steps: 0 A cm^{-2}, 0.025 A cm^{-2}, 0.05–0.5 A cm^{-2} in steps of 0.05 A cm^{-2}, 1–6.5 A cm^{-2} with a step size of 0.5 A cm^{-2} and from 7 A cm^{-2} on the current density was increased in steps of 1 A cm^{-2}. To ensure a complete cell conditioning, both conditioning procedure and polarization measurements were performed for two times. In the results and discussion part always the second polarization curve is shown. In order to investigate stability in a full cell setup, a 100 h constant current hold at 1 A cm^{-2} was performed, followed by recording a third polarization curve. The HFR was measured in parallel at a frequency of 1000 Hz.

Electrochemical Stability and Activity Measurements: To assess the activation and stability behavior of the synthesized Mo_3S_{13}-NCNT catalyst, a SFC setup was connected to an ICP MS.[46,47] SFC electrochemical experimentation was carried out with a LabVIEW-controlled Gamry Reference 600 potentiostat (Gamry, USA), comprising a double-junction Ag/AgCl reference electrode compartment (Metrohm, Switzerland; outer compartment filled with 0.1 M $HClO_4$, inner compartment with standard 3 M KCl electrolyte) and a graphite rod counter electrode compartment (6 mm diameter, 99.995%, Sigma-Aldrich). The V-shaped SFC employed here (WE area: 0.033 cm^2) was manufactured in-house by computerized numerical control (CAM 4-02 Impression Gold, vhf camfacture AG, Germany) machining from a polycarbonate block.

For electrocatalyst testing with the SFC system, 0.2 µL of $[Mo_3S_{13}]^{2-}$ and Mo_3S_{13}-NCNT inks were dropcasted as catalyst spots (Ø ≈ 1.3 mm) onto a mirror-polished 5 cm × 5 cm glassy carbon plate (HTW, SIGRADUR), giving a loading per spot of ≈90 µgcat cm^{-2}. Inks were prepared by dispersing 6.03 mg and 5.8 mg of $[Mo_3S_{13}]^{2-}$ and Mo_3S_{13}-NCNT powders into a mixed solvent. The mixed solvent contained a 87.5/12.5 v/v ratio of ultrapure water (Merck, Milli-Q IQ 7000, 18,2 MΩ cm)/isopropanol (Merck, Emsure) and a Nafion solution (5 wt%, Sigma-Aldrich) to yield a catalyst-to-ionomer weight ratio of 11/1 (final ink concentration = 5.65 g L^{-1}, Nafion contribution to total solid content ≈9%). To ensure homogeneous inks, the suspensions were sonicated with an ultrasonication horn (Branson, SFX 150) during 10 min at 4 s/2 s on/off pulse intervals and 40% pulse amplitude in an ice bath. To perform electrochemical experiments, the SFC was vertically aligned to the position of the catalyst spots by means of a vertical camera.

During experimentation, the SFC cell setup was connected to a Perkin Elmer NexION 350x ICP-MS with Tygon tubing (internal diameter: 1.02 mm) to enable real time quantification of potential-dependent catalyst dissolution; further setup details can be found in refs. [46,47]. The ICP-MS instrument was calibrated with four standard solutions containing intentional amounts of Mo (Merck Certipur) using 10 µg L^{-1} 103Rh as internal standard. A freshly prepared 0.1 M $HClO_4$ electrolyte (70%, Suprapur, Merck; pH = 1) with ultrapure water was pumped from a reservoir connected to the SFC setup downstream toward the ICP-MS, at a flow rate of 215 µL min^{-1}.

Supporting Information

Supporting Information is available from the Wiley Online Library or from the author.

Acknowledgements

P. K. R. Holzapfel and M. Bühler contributed equally to this work. The authors acknowledge the financial support of the Federal Ministry of Education and Research of Germany in the framework of Power-MEE (03SF0536F and 03SF0536E). This work was also partially funded within the project CREATE by the European Union's Horizon 2020 research and innovation program under Grant Agreement No. 721065. The authors further acknowledge Claudia Schwarz for valuable scientific discussions. Open access funding enabled and organized by Projekt DEAL.

Conflict of Interest

The authors declare no conflict of interest.

Keywords

hydrogen evolution reaction, molybdenum sulfide, non-noble metal catalysts, porous transport electrodes, proton exchange membrane water electrolysis

Received: May 20, 2020
Revised: July 2, 2020
Published online: August 16, 2020

[1] M. Beaudin, H. Zareipour, A. Schellenberglabe, W. Rosehart, *Energy Sustainable Dev.* **2010**, *14*, 302.
[2] Z. Zhang, R. Miyajima, T. Inada, D. Miyagi, M. Tsuda, *Int. J. Hydrogen Energy* **2018**, *43*, 6879.
[3] J. Yan, T. Shamim, S. K. Chou, U. Desideri, H. Li, *Appl. Energy* **2017**, *185*, 953.
[4] J. Wang, *Appl. Energy* **2017**, *189*, 460.
[5] *PEM Electrolysis for Hydrogen Production: Principles and Applications* (Eds: D. G. Bessarabov, H. Wang, H. Li, N. Zhao), CRC Press, Boca Raton, FL **2016**.
[6] U. Babic, M. Suermann, F. N. Büchi, L. Gubler, T. J. Schmidt, *J. Electrochem. Soc.* **2017**, *164*, F387.
[7] M. Espinosa-López, C. Darras, P. Poggi, R. Glises, P. Baucour, A. Rakotondrainibe, S. Besse, P. Serre-Combe, *Renewable Energy* **2018**, *119*, 160.
[8] J. Koponen, A. Kosonen, V. Ruuskanen, K. Huoman, M. Niemelä, J. Ahola, *Int. J. Hydrogen Energy* **2017**, *42*, 29648.
[9] M. Carmo, D. L. Fritz, J. Mergel, D. Stolten, *Int. J. Hydrogen Energy* **2013**, *38*, 4901.
[10] M. Suermann, A. Pătru, T. J. Schmidt, F. N. Büchi, *Int. J. Hydrogen Energy* **2017**, *42*, 12076.
[11] S. E. Hosseini, M. A. Wahid, *Renewable Sustainable Energy Rev.* **2016**, *57*, 850.
[12] M. Bernt, A. Siebel, H. A. Gasteiger, *J. Electrochem. Soc.* **2018**, *165*, F305.
[13] E. Fabbri, A. Habereder, K. Waltar, R. Kötz, T. J. Schmidt, *Catal. Sci. Technol.* **2014**, *4*, 3800.
[14] C. Rozain, E. Mayousse, N. Guillet, P. Millet, *Appl. Catal., B* **2016**, *182*, 123.
[15] N. Han, K. R. Yang, Z. Lu, Y. Li, W. Xu, T. Gao, Z. Cai, Y. Zhang, V. S. Batista, W. Liu, X. Sun, *Nat. Commun.* **2018**, *9*, 924.
[16] M. Huynh, C. Shi, S. J. L. Billinge, D. G. Nocera, *J. Am. Chem. Soc.* **2015**, *137*, 14887.
[17] I. A. Moreno-Hernandez, C. A. MacFarland, C. G. Read, K. M. Papadantonakis, B. S. Brunschwig, N. S. Lewis, *Energy Environ. Sci.* **2017**, *10*, 2103.
[18] H. Yang, Y. Zhang, F. Hu, Q. Wang, *Nano Lett.* **2015**, *15*, 7616.
[19] J. W. D. Ng, T. R. Hellstern, J. Kibsgaard, A. C. Hinckley, J. D. Benck, T. F. Jaramillo, *ChemSusChem* **2015**, *8*, 3512.
[20] H. Kim, E. Hwang, H. Park, B.-S. Lee, J. H. Jang, H.-J. Kim, S. H. Ahn, S.-K. Kim, *Appl. Catal., B* **2017**, *206*, 608.
[21] J. D. Benck, T. R. Hellstern, J. Kibsgaard, P. Chakthranont, T. F. Jaramillo, *ACS Catal.* **2014**, *4*, 3957.
[22] A. Gomez Vidales, S. Omanovic, *Electrochim. Acta* **2018**, *262*, 115.
[23] D. Escalera-López, Z. Lou, N. V. Rees, *Adv. Energy Mater.* **2019**, *9*, 1802614.
[24] B. Hinnemann, P. G. Moses, J. Bonde, K. P. Jørgensen, J. H. Nielsen, S. Horch, I. Chorkendorff, J. K. Nørskov, *J. Am. Chem. Soc.* **2005**, *127*, 5308.
[25] T. Corrales-Sánchez, J. Ampurdanés, A. Urakawa, *Int. J. Hydrogen Energy* **2014**, *39*, 20837.
[26] J. H. Kim, H. Kim, J. Kim, H. J. Lee, J. H. Jang, S. H. Ahn, *J. Power Sources* **2018**, *392*, 69.
[27] A.-Y. Lu, X. Yang, C.-C. Tseng, S. Min, S.-H. Lin, C.-L. Hsu, H. Li, H. Idriss, J.-L. Kuo, K.-W. Huang, L.-J. Li, *Small* **2016**, *12*, 5530.
[28] S. M. Senthil Kumar, K. Selvakumar, R. Thangamuthu, A. Karthigai Selvi, S. Ravichandran, G. Sozhan, K. Rajasekar, N. Navascues, S. Irusta, *Int. J. Hydrogen Energy* **2016**, *41*, 13331.
[29] L. A. King, M. A. Hubert, C. Capuano, J. Manco, N. Danilovic, E. Valle, T. R. Hellstern, K. Ayers, T. F. Jaramillo, *Nat. Nanotechnol.* **2019**, *14*, 1071.
[30] C. V. Pham, A. Zana, M. Arenz, S. Thiele, *ChemElectroChem* **2018**, *5*, 2672.
[31] P. D. Tran, T. V. Tran, M. Orio, S. Torelli, Q. D. Truong, K. Nayuki, Y. Sasaki, S. Y. Chiam, R. Yi, I. Honma, J. Barber, V. Artero, *Nat. Mater.* **2016**, *15*, 640.
[32] J. Kibsgaard, T. F. Jaramillo, F. Besenbacher, *Nat. Chem.* **2014**, *6*, 248.
[33] Y. Li, H. Wang, L. Xie, Y. Liang, G. Hong, H. Dai, *J. Am. Chem. Soc.* **2011**, *133*, 7296.
[34] K. Zhang, Y. Zhao, S. Zhang, H. Yu, Y. Chen, P. Gao, C. Zhu, *J. Mater. Chem. A* **2014**, *2*, 18715.
[35] D. Y. Chung, S. Park, P. P. Lopes, V. R. Stamenkovic, Y.-E. Sung, N. M. Markovic, D. Strmcnik, *ACS Catal.* **2020**, *10*, 4990.
[36] M. Ledendecker, J. S. Mondschein, O. Kasian, S. Geiger, D. Göhl, M. Schalenbach, A. Zeradjanin, S. Cherevko, R. E. Schaak, K. Mayrhofer, *Angew. Chem., Int. ed. Engl.* **2017**, *56*, 9767.
[37] M. Pourbaix, *Atlas of Electrochemical Equilibria in Aqueous Solutions*, National Association of Corrosion Engineers, Houston, TX **1974**.
[38] S. Cherevko, S. Geiger, O. Kasian, N. Kulyk, J.-P. Grote, A. Savan, B. R. Shrestha, S. Merzlikin, B. Breitbach, A. Ludwig, K. J. J. Mayrhofer, *Catal. Today* **2016**, *262*, 170.
[39] D. W. Redman, M. J. Rose, K. J. Stevenson, *Langmuir* **2017**, *33*, 9354.
[40] Y. Deng, L. R. L. Ting, P. H. L. Neo, Y.-J. Zhang, A. A. Peterson, B. S. Yeo, *ACS Catal.* **2016**, *6*, 7790.
[41] H. Vrubel, X. Hu, *ACS Catal.* **2013**, *3*, 2002.
[42] H. G. S. Casalongue, J. D. Benck, C. Tsai, R. K. B. Karlsson, S. Kaya, M. L. Ng, L. G. M. Pettersson, F. Abild-Pedersen, J. K. Nørskov, H. Ogasawara, T. F. Jaramillo, A. Nilsson, *J. Phys. Chem. C* **2014**, *118*, 29252.
[43] P. Holzapfel, M. Bühler, C. van Pham, F. Hegge, T. Böhm, D. McLaughlin, M. Breitwieser, S. Thiele, *Electrochem. Commun.* **2020**, *110*, 106640.
[44] M. Klingele, M. Breitwieser, R. Zengerle, S. Thiele, *J. Mater. Chem. A* **2015**, *3*, 11239.
[45] M. Bühler, P. Holzapfel, D. McLaughlin, S. Thiele, *J. Electrochem. Soc.* **2019**, *166*, F1070.
[46] S. O. Klemm, A. A. Topalov, C. A. Laska, K. J. J. Mayrhofer, *Electrochem. Commun.* **2011**, *13*, 1533.
[47] *Encyclopedia of Interfacial Chemistry: Surface Science and Electrochemistry* (Ed: K. Wandelt), Elsevier, Amsterdam **2018**.